Volume 18, Number 2, 2025. pp. 183-196

Jordan Journal of Physics

ARTICLE

Growth and Properties of Pure Phase Kesterite CZTS Nanostructure for Electrochemical, Photocatalytic, and Antibacterial Applications

S. Manjula[a], **A. Sarathkumar**[a], **S. Nithishkumar**[a], **G. Sivakumar**[b] and **K. Mohanraj**[c]

[a] *Department of Science and Humanities-Physics, Krishnasamy College of Engineering and Technology, Tamil Nadu 607 109, India.*

[b] *CISL, Annamalai University, Tamil Nadu, 608 002 India.*

[c] *Department of Physics, School of Basic and Applied Sciences, Centra University of Tamil Nadu, Thiruvarur - 610 101, India.*

Doi: **https://doi.org/10.47011/18.2.8**

Received on: 23/11/2023; *Accepted on: 17/04/2024*

Abstract: Surfactant-free, high-grade, self-assembled quaternary copper zinc tin sulfide (CZTS) nanoparticles were synthesized successfully via a simple hydrothermal method. Different thiourea concentrations were used as chalcogen precursors, and their influences were investigated. The concentration of sulfur precursor gradually increased to obtain a pure kesterite phase, which was identified by X-ray diffractometer (XRD) and Fourier-transform Raman spectrometer (FT-Raman). Field emission scanning electron microscopy (FESEM) revealed diverse nanostructures, such as spheres, plates, and rose-like formations. The specific capacitance values of pure-phase kieserite CZTS nanoparticles were analyzed using a three-electrode system. The photocatalytic activity of CZTS nanoparticles against methylene blue (MB) and crystal violet (CV) degradation under visible light irradiation reached 93% and 89% within 70 min, respectively. Also, CZTS TU-10 nanostructures exhibited stronger antibacterial performance against both gram-positive (*Streptococcus pneumoniae, Streptococcus pyogenes*) and gram-negative (*Klebsiella pneumoniae, Vibrio parahaemolyticus*) pathogens. The maximum inhibition zone (26 mm) was obtained against *Vibrio parahaemolyticus* bacteria using the agar well diffusion method. These results imply that kesterite CZTS could be considered an efficient candidate for multiple applications.

Keywords: CZTS, Hydrothermal, Morphology, Electrochemical, Specific capacitance.

1. Introduction

Cu_2ZnSnS_4 (CZTS) is a p-type semiconducting material with promising potential for thermoelectric, photocatalytic, and energy harvesting applications [1]. Although CZTS nanoparticle synthesis has been reported already, some significant problems remain. The formation of these compounds is complicated by the multiple components that go into their production [2]. Due to the intrinsically small composition zone for a single-phase CZTS, the simplicity of component vaporization, and the high chemical potential for secondary phase formation, the formation of a pure single-phase structure of this product is challenging [3, 4]. Surfactant-free synthesis methods employing different sulfur sources and concentrations have received limited attention [5]. CZTS nanoparticles have been synthesized by hydrothermal, sol-gel [6], solvothermal [7], SILAR [8], hot injection [9], and pulsed laser deposition methods. Among these techniques, hydrothermal treatment is the most important due to its simple process, low cost, environmental friendliness, and control over the

Corresponding Author: G. Sivakumar **Email**: gskdopcisl@gmail.com

structure and morphology of the material [10]. Electrochemical supercapacitors are gaining much attention among the various energy storage technologies because of their exceptional durability [11], elevated energy and power density, expedited redox processes for charging and discharging, environmentally sustainable attributes, and cost-effectiveness [12]. However, limited research has focused on the electrochemical behavior and energy storage applications of CZTS nanostructures [13].

Hence, in the present work, we propose a facile one-step hydrothermal method for the preparation of kesterite CZTS nanostructures. The novelty of the present work lies in the surfactant-free synthesis of single-phase CZTS nanoparticles. A key objective is to investigate the effect of varying sulfur precursor concentrations on the phase formation of CZTS. Also, this study explores the specific capacitance of CZTS nanostructures through cyclic voltammetry (CV) and GCD charge-discharge techniques. The photocatalytic degradation of CZTS is tested using two different dyes. The antibacterial activity of CZTS nanostructure is examined against gram-positive and gram-negative bacteria.

2. Materials and Methods

Copper chloride dihydrate, zinc nitrate hexahydrate, and stannous chloride dihydrate were used as metal precursors for Cu, Zn, and Sn, respectively. For the sulfur source, thiourea was used. All the compounds were acquired from Lakshmi Scientific Company, Chidambaram, India, AR grade, and used without purification. Polyvinylidene fluoride (PVDF), carbon black, N-methyl 2-pyrrolidone solution (NMP), and nickel plate were purchased from Sabari Scientific Company, Tamil Nadu, India, for electrochemical processing.

2.1 Hydrothermal Synthesis of CZTS Nanostructures

To synthesize CZTS nanostructures by a hydrothermal method, thiourea (TU) was used as a sulfur source. In a typical synthesis of CZTS nanostructures (TU-4), the molar ratio (Cu:2, Zn:1, Sn:1, Tu:4) was taken as follows: 0.08 M copper chloride dihydrate (0.136 g/10 ml), 0.04 M zinc nitrate hexahydrate (0.059 g/5 ml), 0.04 M stannous chloride dihydrate (0.045 g/5 ml), and 0.16 M thiourea (TU - 0.243 g/20 ml). A solution was prepared using distilled water and stirred for 30 min. The resulting solution was transferred into a Teflon-lined stainless-steel autoclave and heated in a muffle furnace at 210 °C for 24 hours, as described in our earlier work [14]. After the reaction, the autoclave was allowed to cool naturally to room temperature. The obtained precipitate was cleaned using distilled water and ethanol and dried for 3 hours in a hot air oven at 70°C. The synthesis was performed without the addition of any surfactants or stabilizing/binding agents. Because of the high temperature used during the synthesis of CZTS nanoparticles, more thiourea was added to compensate for the amount that evaporated. To examine the growth and properties of pure phase kesterite Cu_2ZnSnS_4 nanostructure by using different sulfur/copper concentrations (S/Cu = 2, 3, 4, and 5) on the structural, phase formation, and morphological features of CZTS nanostructures, the above procedure was followed to synthesize TU-6 (2:1:1:6), TU-8 (2:1:1:8), and TU-10 (2:1:1:10) samples.

2.2 Characterization

The crystal structure and phase composition of the synthesized CZTS nanostructures were characterized by X-ray diffraction (XRD) using a PANalytical X'Pert PRO – Analytic, Germany, operated at 30 mA and 40 kV with Cu Kα radiation (λ = 1.54060Å). Phase confirmation was further carried out using a micro-laser Raman spectrometer (Seiki, Japan) at Alagappa University, Karaikudi.

Surface morphology and elemental composition were analyzed by field emission scanning electron microscopy (FESEM, Carl Zeiss Sigma 300) equipped with energy-dispersive X-ray spectroscopy (EDAX) at CISL, Annamalai University, Chidambaram. Transmission electron microscopy (TEM) was performed using a Tecnai G2 20 S-Twin (200 kV, Japan) at Madurai Kamaraj University, Madurai, to further study the structural properties.

2.2.1. Preparation of the CZTS electrode

To prepare the electrode, a slurry paste was obtained by mixing 80 wt.% CZTS powder, 10 wt.% PVDF, and 10 wt.% carbon black, with N-methyl-2-pyrrolidone (NMP) added dropwise until a uniform paste was formed. This slurry was coated onto a nickel plate (1 cm × 1 cm active area) and dried overnight at 80 °C. The

mass of active material on the electrode was approximately 5 mg. The electrochemical performance was evaluated using a three-electrode system consisting of the prepared CZTS electrode as the working electrode, a platinum wire as the counter electrode, and an Ag/AgCl electrode as the reference electrode. A 2 M KOH aqueous solution was used as the electrolyte.

2.2.2 Electrochemical Performance of the Supercapacitor

The electrochemical characteristics of CZTS nanoparticles were investigated by the cyclic voltammetry technique using a Metrohm Autolab M204 system and a three-electrode cell system with NOVA 2.1.4 software at Annamalai University. Cyclic voltammetry measurements calculated the specific capacitance of the CZTS electrode in the range of a potential window of 0 to 0.6 mV/s with varying scan rates. GCD analysis was performed at different current densities. To determine the specific capacitance (C_{sp}) of the CZTS electrode,[the following equations were used [15].

For cyclic voltammetry:

$$C_{sp} = \frac{\int I \Delta v}{Sm\Delta v} \text{F/g} \quad (1)$$

For GCD:

$$C_{sp} = \frac{Idt}{mdV} \text{F/g} \quad (2)$$

where C_{sp} (Fg^{-1}) is the specific capacitance, $\int I \Delta t$ is the area of the CV curve, s is the scan rate (mV/s), ΔV is the potential window (V), m is the mass of the loaded material (g), I is the current density (A), dt is the discharge time (s), g is the mass of the loaded material, and 'dV' is the potential (V).

2.2.3. Photocatalytic Measurements

The degradation of methylene blue (MB) and crystal violet (CV) dyes in an aqueous solution was used under sunlight as a radiation source. The photocatalytic reaction of the CZTS was measured by using a UV-Vis spectrophotometer. The optimal concentration for the dye is 10^{-4} mol. Blank solutions were prepared by dissolving the dye in 1 liter of distilled water. Initially, 0.05 g of prepared CZTS nanoparticles was added to 100 ml of blank dye solutions. To achieve adsorption-desorption equilibrium between the catalyst (CZTS) and dye, a beaker containing the dye solution and the catalyst was left in dark conditions for 30 minutes. The pH of the MB and CV dye solutions was recorded during photocatalytic activity. For the degradation of dyes, both solutions were stirred separately under sunlight. Every 10 minutes, 5 mL of the solution was collected from the beaker for UV-visible analysis.

2.3 Antibacterial Activity

The CZTS nanoparticles offer the advantages of low toxicity and significant antibacterial activity at low concentrations, all of which are needed for these nanomaterials to act as potent antimicrobial agents inside most living systems [16]. The CZTS was tested for its antibacterial properties by using the agar well diffusion method.

3. Results and Discussion

3.1 Structural Analysis

Structural characteristics of CZTS nanoparticles were analyzed by XRD for different concentrations of thiourea, and the results are presented in Figs. 1(a)-1(d). As seen in Fig. 1(a), the diffraction peaks of TU-4 at 29.07°, 31.53°, and 32.56° are attributed to (102), (103), and (006) hkl planes of CuS binary phase with the hexagonal system (JCPDS: 78-2121). The presence of other peaks at 2θ = 47.53° and 59.12° corresponds to (220) and (224) planes, confirming the presence of the CZTS phase with the tetragonal system (JCPDS: 26-0575) [17]. By increasing the TU concentration to TU-6 and TU-8, the intensity of characterization peaks of CZTS at 2θ = 28.49°, 47.27°, 56.66°, and 59.31° corresponding to the (112), (220), (312), and (224) planes increased. Additionally, the plane corresponding to (102), (103), (006), and (108) of CuS decreased gradually, while peaks related to the CuS phase (e.g., (102), (103), (006), and (108)) gradually diminished. At the highest thiourea concentration (TU-10), the CuS peaks disappeared entirely, and only prominent CZTS peaks were observed at 2θ = 28.42°, 47.58°, 56.14°, and 59.26°, confirming the successful formation of a pure kesterite phase. This indicates that an increased sulfur precursor is essential to suppress secondary phase formation due to sulfur evaporation at elevated temperatures during hydrothermal synthesis [18]. The crystallite size (D) was calculated using Eq.(3), [19]:

$$D = \frac{k\lambda}{\beta cos\theta} \quad (3)$$

The calculated crystallite sizes were 52 nm (TU-4), 45 nm (TU-6), 36 nm (TU-8), and 28 nm (TU-10), indicating the nanocrystalline nature of all samples. The small crystallite sizes indicated that the synthesized CZTS samples were nano-crystalline. Lattice parameters a = b and c ranged from 5.432 to 5.426 Å and 10.853 to 10.842 Å, respectively, in agreement with standard JCPDS values. These results demonstrate that the sulfur concentration significantly influences the structural parameters and phase purity of CZTS nanostructures.

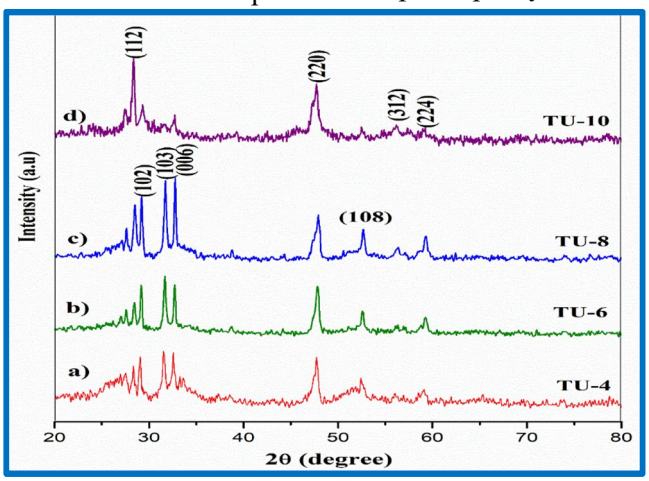

FIG. 1. XRD patterns of CZTS nanoparticles at different concentrations of thiourea (TU).

3.2. Raman Analysis

Raman analysis was carried out to confirm the appearance of minor phases and the phase purity of CZTS nanostructures. The Raman spectra of CZTS nanostructures with different concentrations of TU are shown in Figs. 2(a)-2(d). For the TU-4 sample, a strong Raman peak was observed in the range of 440–465 cm^{-1}, indicating the presence of a CuS secondary phase [4]. When thiourea concentrations were increased to TU-6, the Raman spectra exhibited one additional peak located at 323 cm^{-1}, which was attributed to the CZTS phase. Harinipriya *et al*. and Shalabayev *et al*. reported similar types of results and stated that kesterite CZTS showed Raman peaks at 338 cm^{-1} [5]. The characteristic peak (CZTS) intensity increased with the increasing sulfur concentration of sample TU-8 because the crystal structure of the synthesized CZTS was strongly affected by the initial formation of copper sulfide, which acts as a catalyst for CZTS growth [3]. With further increase in sulfur concentration (TU-10), the peak corresponding to the mixed phase, namely, CuS (467 cm^{-1}), vanished, and the intensity of the peak corresponding to CZTS (338 cm^{-1}) increased gradually. The exclusive presence of kesterite CZTS peaks in the TU-10 sample confirms the successful suppression of secondary phases. This high phase purity is particularly advantageous for photocatalytic and electrochemical applications.

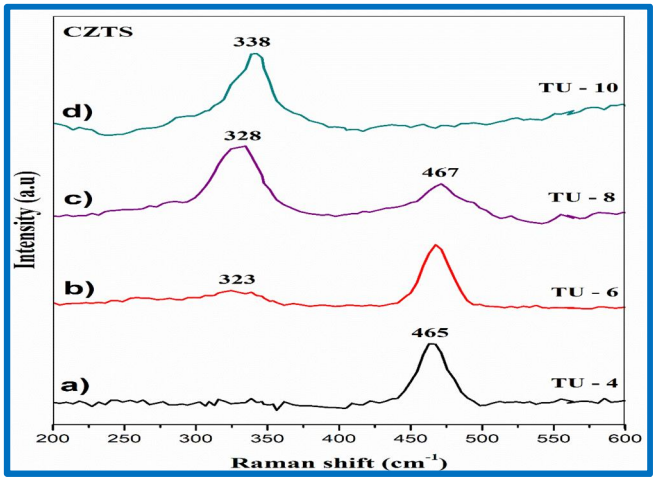

FIG. 2. Raman spectra of CZTS with different TU concentrations.

In addition, intermediate phases such as Cu_3SnS_4 (318 and 295 cm^{-1}), ZnS_2 (315 cm^{-1}), and SnS_2 (351 and 274 cm^{-1}) were not detected in the Raman spectra, indicating that the pure phase of CZTS nanostructures was observed at higher concentration. These results confirmed that the synthesized CZTS TU-10 nanostructure exhibited a pure Raman peak compared to other samples. A similar type of result was obtained from the XRD study.

3.3. Morphological Analysis

The lower (a) and higher (b) magnified FESEM images and EDS spectra (c) with atomic ratio (pie chart) of CZTS samples for different TU concentrations are shown in Figs. 3i-3iv. These analyses were performed to reveal the morphology and microstructural characteristics of the CZTS nanoparticles.

The lower concentration (Fig. 3i) of the TU-4 sample is heterogeneous (plate-like, cubical, and rod-like) in nature. In TU-6 (Fig. 3ii), many hierarchical spherical-like structures, typically measuring 1-2µm in size, are noticed. Upon further increasing the concentration (TU-8), the sphere-like structure changed to hexagonal nanosheets with an approximate thickness of 30-40 nm, attached as a bundle-like formation. At higher TU concentration (TU-10, Fig. 3iv), a well-defined rose-flower-like morphology was observed, composed of interlinked hexagonal nanosheets with an overall particle size in the range of 1–3 µm. The nanosheets result in numerous hierarchical pores on the nanoscale. Fig. 3iv(c) shows the EDS spectrum of the TU-10 sample with the inset depicting the average atomic ratio of the four elements. The atomic ratio of Cu:Zn:Sn:S was found to be 20.70:9.79:15.15:54.36, which is close to the stoichiometric ratio of Cu_2ZnSnS_4 and well matched with the XRD analysis. Table 1 reveals the different elemental composition atomic ratios of different TU concentrations.

The formation of the self-assembled flower-like CZTS nanostructure at high TU concentrations is proposed to occur via the following stages: initially, 1D CZTS nanoparticles form through homogeneous nucleation. These subsequently grow into 2D nanosheets through oriented aggregation, and eventually self-assemble into 3D rose-flower-like architectures via the Ostwald ripening mechanism [21]. This hierarchical structure, with nanosheets as the primary building block, is advantageous due to its large surface area and high aspect ratio, which are beneficial for enhancing electrochemical performance, as reported in previous studies [22].

The gradual release of S^{2-} ions from thiourea and the interaction between the $–NH_2$ groups of thiourea and CZTS nanoparticles are believed to facilitate these stepwise growth processes [21]. Furthermore, the absence of extraneous elements in the EDS spectra confirmed the successful formation of pure-phase CZTS nanostructures.

FE-SEM analysis of the TU-10 sample clearly highlights the influence of sulfur source and sulfur concentration on the size, nucleation extent, morphological changes, and structure of the synthesized CZTS nanostructures. The presence of flower-like morphology with hierarchical pore structure of CZTS nanoparticles confirms the synthesis of phase-pure CZTS, supported by the XRD and Raman studies as well. Hence, further characterization and application studies were carried out using CZTS TU–10 alone.

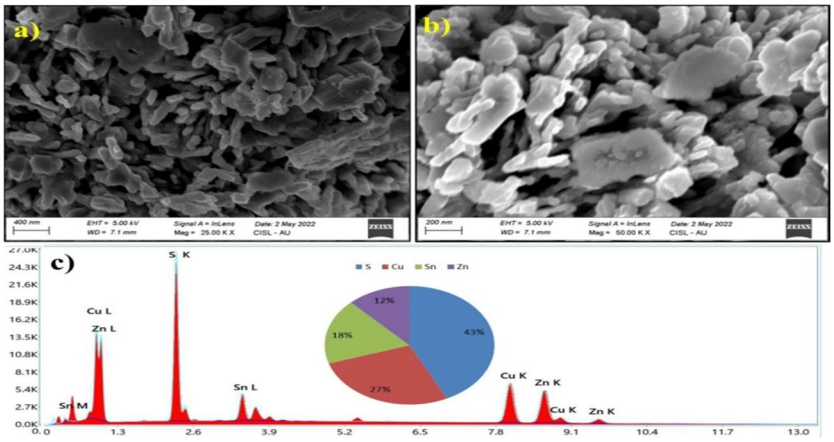

FIG. 3i. FESEM images of TU-4 at (a) lower and (b) higher magnification. (c) EDS spectrum with atomic ratio (inset pie chart).

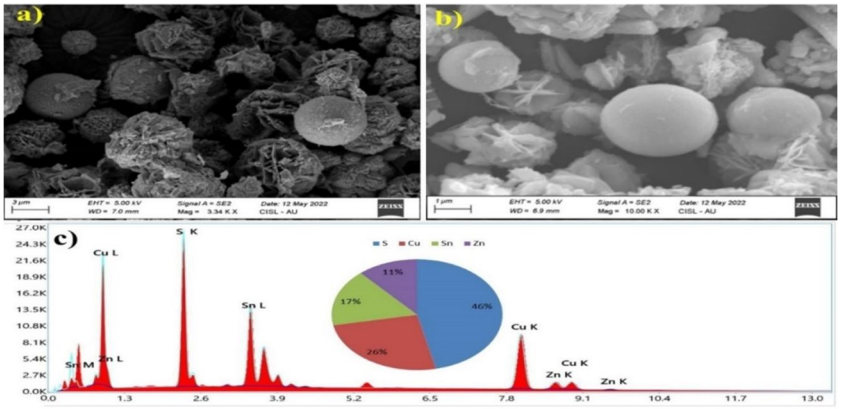

FIG. 3ii. FESEM images of TU-6.

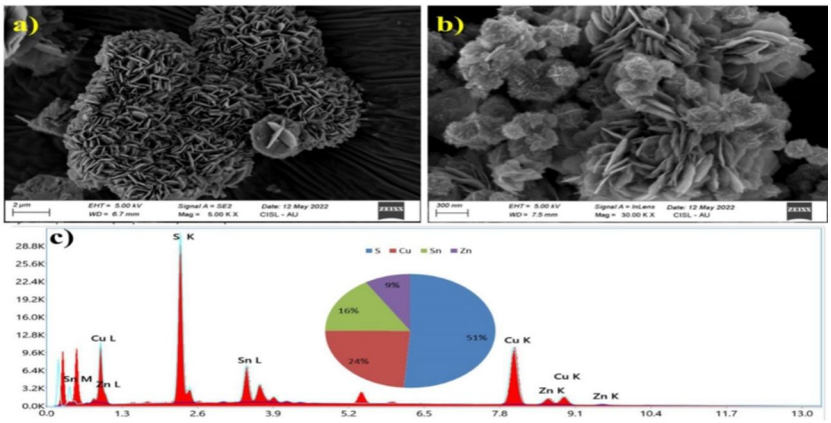

FIG. 3iii. FESEM images of TU-8.

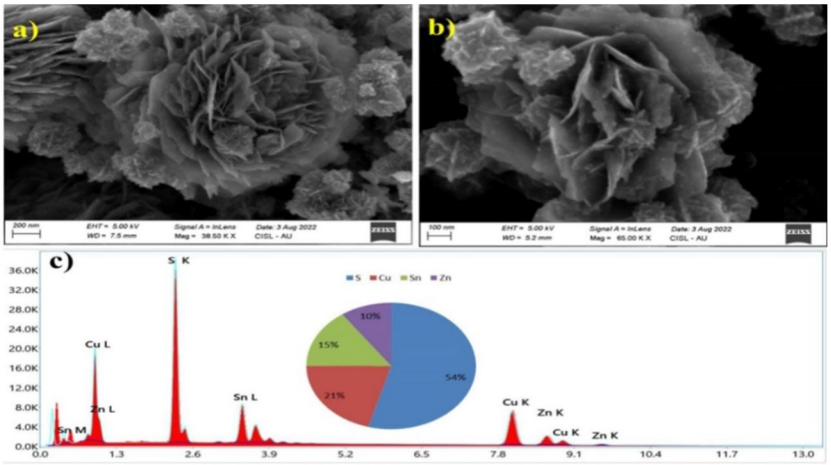

FIG. 3iv. FESEM images of TU-10.

TABLE 1. EDS analysis of CZTS recorded at different TU concentrations.

Composition Ratio (at %)	Sample			
	TU-4	TU-6	TU-8	TU-10
Cu	27.30	25.50	23.80	20.70
Zn	12.14	11.49	8.75	9.79
Sn	17.82	16.56	16.20	15.15
S	42.74	46.45	23.80	54.36
Cu/Zn+Sn	0.91	0.90	0.95	0.82
Zn/Sn	0.68	0.69	0.54	0.64
S/(Cu+Zn+Sn)	0.74	0.86	1.05	1.19
S/Cu	1.56	1.82	2.15	2.62

3.4. Transmission Electron Microscopy (TEM)

The structural and morphological characteristics of the CZTS TU-10 sample were further examined using high-resolution transmission electron microscopy (HRTEM). The different magnifications of the TEM images of the CZTS TU-10 nanostructures are depicted in Figs. 4(a)-4(d) and reveal that the nanoparticles are well dispersed with a rose flower-like structure. The average size of the flower-like structures is approximately 1-2 µm. As seen in Fig. 4(a), the flower-like morphology consists of interconnected nanosheets, consistent with the FESEM results. The number of hexagonal sheets that are less than 50 nm arranged together to form the flower-like structure, which is visually evident from Figs. 4(c)-4(d). Fig. 4(e) shows a single crystalline of the nanosheet that exhibits a lattice fringe value of 0.32 nm corresponding to the (112) plane of CZTS, which seems to be close to the earlier report by [23]. The bright spots in the SAED pattern in Fig. 4(f) corresponding to the (112), (220), and (224) planes were found to be consistent with the planes observed by XRD. The presence of four diffraction rings indicates that the nanoparticles are well crystallized, and the results witness the presence single crystal of pure-phase CZTS nanoparticles.

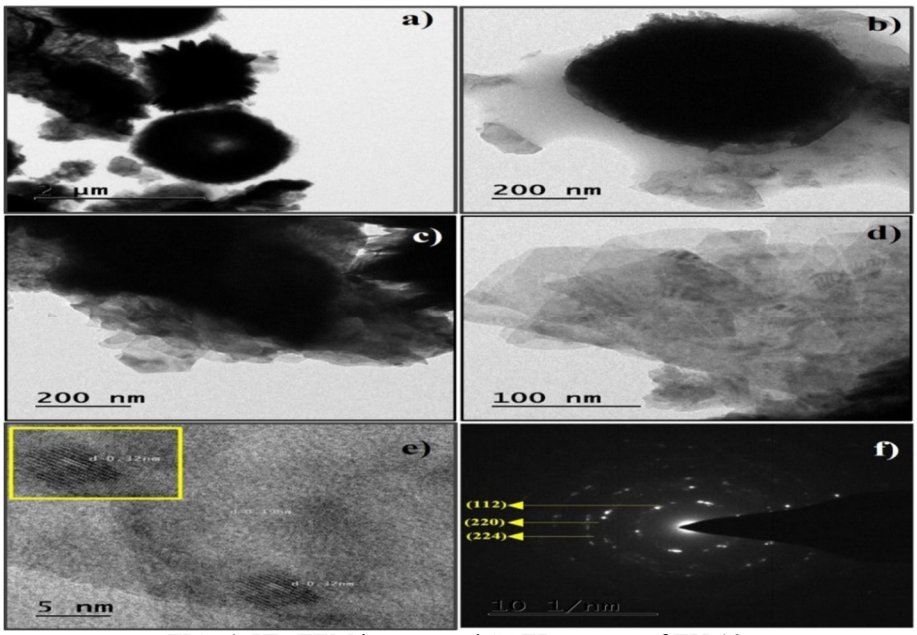

FIG. 4. HR-TEM images and SAED pattern of TU-10.

3.5. XPS Analysis

The CZTS TU-10 sample was examined using X-ray photoelectron spectroscopy to confirm the important information on the surface level, its chemical composition, and valence states. Fig. 5(a) depicts the survey scan spectrum of the CZTS sample, which includes Cu, Zn, Sn, and S. The peak at 284.6 eV C1s is used as a reference, and the peak at 532.9 eV is O1s corresponding to the water molecule at the surface of the sample [24].

High-resolution XPS spectrum of Cu 2p peaks, seen in Fig. 5(b), was found in the binding energies of Cu $2p_{3/2}$ and Cu $2p_{1/2}$ peaks at 933.8 and 953.7 eV, respectively, with a peak separation of 20.1 eV [19]. The observed results confirmed that the oxidation state of Cu is +1. For Zn, peaks split into two energy states, Zn $2p_{3/2}$ and Zn $2p_{1/2,}$ and detected at 1021.9 and 1044.9 eV, respectively, with the distance between the two peaks at 23 eV, as seen in Fig. 5(c). The obtained result proved that Zn is present in an oxidation state of +2 [25]. The Sn peaks observed in Fig. 3.5(d) are found at binding energies of 486.2 and 494.4 eV and could be attributed to the Sn $3d_{5/2}$ and Sn $3d_{3/2}$ peaks, which match the conventional splitting of 8.2 eV [26]. As shown in Fig. 5(e), the S 2p peaks were successfully deconvoluted into two distinct peaks. The primary peaks located at 164.8 eV and the secondary peaks detected at 165.9 eV were assigned for $2p_{3/2}$ and $2p_{1/2}$, and the difference is 1.1 eV, corresponding to S^{2-} [27]. The obtained valence states of Cu^{1+}, Zn^{2+}, Sn^{4+}, and S^{2-} provide evidence that the prepared CZTS TU-10 sample was in good agreement with the pure phase kesterite Cu_2ZnSnS_4.

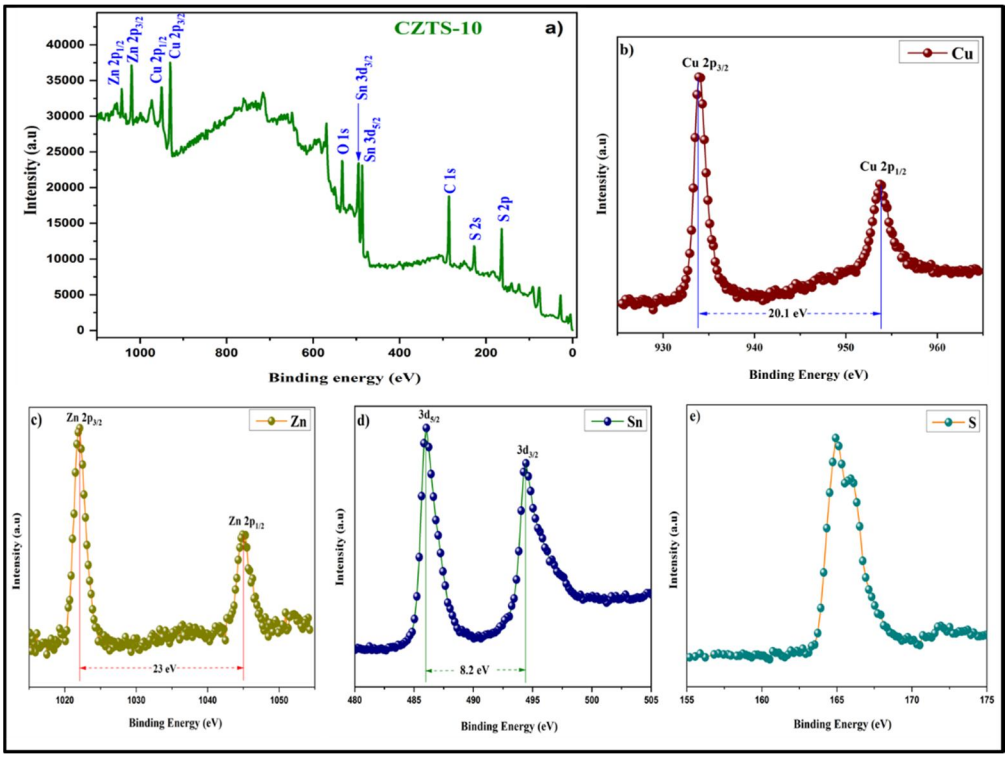

FIG. 5. XPS spectra of CZTS TU-10 nanostructures. (a) Survey scan spectrum, (b) Cu, (c) Zn, (d) Sn, and (e) S.

3.6. Optical Properties

To estimate the value of the direct bandgap, the optical absorption characteristics of CZTS TU-10 were investigated by using UV-Vis spectroscopy in the 200-800 nm wavelength range. Fig. 6(a) shows the presence of a strong absorption spectrum, suggesting that the CZTS TU-10 sample exhibited significant potential application in photocatalytic measurements [28]. By using Tauc's plot [29], the optical bandgap of CZTS TU-10 nanostructure was determined for direct bandgap energy:

$$\alpha h\nu = A(h\nu - E_g)^n \quad (4)$$

where hν is the photon energy, Eg is the optical bandgap of the products, A is a constant, and n is 1/2 for the direct bandgap semiconductor. The optical bandgap energy (Eg) of the CZTS sample was calculated by extrapolating the linear portion of $(\alpha h\nu)^2$ on the y-axis versus hν on the x-axis, as shown in the inset of Fig. 5(b) The calculated band gap value of CZTS TU-10 nanostructures was found to be 1.52 eV, which could be attributed to the enhanced ordering within nanocrystals with a better crystalline nature. This value is close to the optimum value for better electrochemical and photocatalytic applications. Furthermore, the obtained band gap value coincides well with the previously reported value [30].

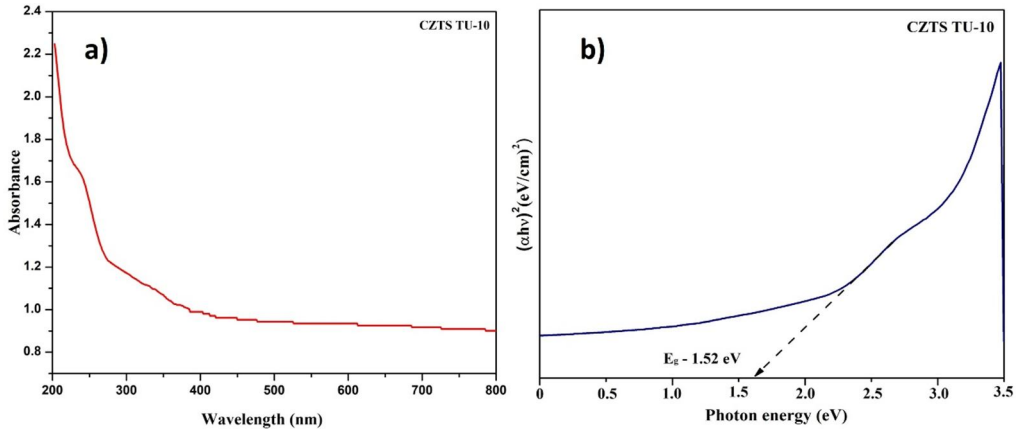

FIG. 6. Optical properties of CZTS TU-10 nanostructures. (a) UV-Vis absorbance, (b) band gap.

3.7. Electrochemical Applications

a) Cyclic Voltammetry

The cyclic voltammetry (CV) curves were obtained for the CZTS TU-10 electrode at 0 to 0.6 V while employing scanning rates ranging from 10 to 100 mV/s. As illustrated in Fig. 7(a), the redox activity of the CZTS TU-10 electrode was confirmed by two redox peaks and shifted in higher positive (oxidation) and lower negative (reduction) potentials as the scan rate increased, which might be related to electric polarization and irreversible reactions [31]. Due to faster kinetics, the CV profiles demonstrated a steady voltammogram shape at increased scan rates, confirming that the electrode material has pseudo-capacitance behavior and better rate performance. The specific capacitance (C_{sp}) of the CZTS TU-10 electrode was calculated using Eq. (1). The calculated C_{sp} values are 389, 290, 232, 179, and 155 F/g for different scan rates of 10, 20, 55, 70, and 100 mV/s, respectively, as shown in Fig. 7(b). Among the scan rates, the lower scan rate has a higher specific capacitance of 389 F/g, which could be attributed to both the inner and outer surfaces involved in tuning the specific capacitance, which results in higher capacitance values [32]. The decrease in specific capacitance with increased scan rates was caused by the rapid redox reaction. While increasing the scan rates, the interplay of various ions at the interface between the electrode and electrolyte was observed at higher scan rates, hence leading to decreased values of Csp.

b) Galvanostatic Charge-Discharge

The specific capacitance of the fabricated electrode was determined by utilizing GCD charge-discharge measurements within the potential range of 0-0.6 V with various current densities (1-5 A/g), as shown in Fig. 7(c). The nonlinear shape of the GCD profile with humbs revealed faradic effects of the constructed electrode for different current density values. The calculated Csp values, calculated using Eq. (2), are found to be 368, 252, 216, 134, and 113 Fg^{-1} for different current densities 1, 2, 3, 4, and 5 Ag^{-1}, respectively. The obtained results indicate that the decreased Csp values were inversely proportional to increasing current densities. This phenomenon could be ascribed to two key factors:
(i) At higher current densities, ion diffusion is limited, preventing full access to the active material;
(ii) Redox reactions are confined mainly to the electrode surface, leading to reduced utilization of active sites [33].

The CZTS TU-10 electrode had a high specific capacitance value of 368 Fg^{-1} for a current density of 1 Ag^{-1} due to the better electrochemical performance with a large surface area. The GCD curve corresponding to 1 Ag^{-1} shows a wide potential plateau. The results discussed above clearly indicate that the sulfur-rich, surfactant-free CZTS TU-10 electrode material will exhibit high performance when utilized in energy storage applications.

c) EIS Spectroscopy

The CZTS TU-10 electrode was subjected to electrochemical impedance spectroscopy (EIS) to examine the fundamental characteristics of the electrode and electrolyte interfaces where charge reactions and ion transfer occur in the system. EIS spectrum was plotted using the real compound (Z') vs imaginary part (Z''), as shown in Fig. 7(d).

The imaginary part (Z'') of the impedance defines the interphase resistance between the working electrode and the electrolyte. The phenomenon of a semicircle transition into a straight line was noticed at higher frequencies. The charge transfer resistance occurs at the interface of the active material as revealed by the small semicircle [34]. The plot shows a large slope in the straight-line part that confirms the CZTS TU-10 electrode has high capacitance and low ion diffusion resistance.

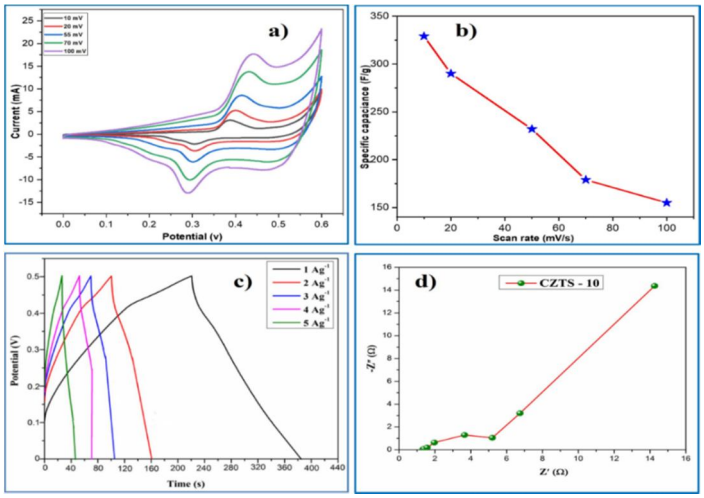

FIG. 7. Electrochemical analysis of CZTS TU-10 nanoparticles. (a) CV, (b) scan rate vs specific capacitance, (c) GCD, and (d) EIS spectrum.

3.8. Photocatalytic Measurements

Figure 8(a) shows the absorption spectra of the CZTS catalyst recorded against the degradation of CV and MB dye solutions under sunlight. The spectra revealed that the maximum absorbance wavelengths of CV and MB dyes were centered at 590 nm and 664 nm, respectively. The absorbance of the solution decreases with increasing time intervals, indicating that the dye concentration decreases as the exposure time increases [35]. The photocatalytic degradation efficiency was evaluated by Eq. (5):

$$\text{Efficiency } (\eta\%) = \left(1 - \frac{C}{C_o}\right) \times 100 \qquad (5)$$

where C and C_o are the initial and final irradiation of the dye solution, respectively. Figs. 8(b) and 9(b) show the absorbance vs time for CV and MB dyes, respectively. The CZTS nanostructures using CV dye had the highest degradation efficiency at 93% [Fig. 8(c)] compared to MB dye at 89% [Fig. 9(c)] within 70 minutes. Fig.s 8(d) and 9(d) show the C/C_0 vs reaction time curves of CV and MB in the presence and absence of a CZTS catalyst. It is well known that a material's large surface area, morphology, crystallinity, and size are crucial to its photocatalytic activity. Consequently, morphology may play a significant role in calculating the final degradation efficiency. In the present work, a flower-like CZTS TU-10 sample exhibited high removal efficiency due to the higher surface area with an optimal particle size of the CZTS catalyst and suitable preparation conditions.

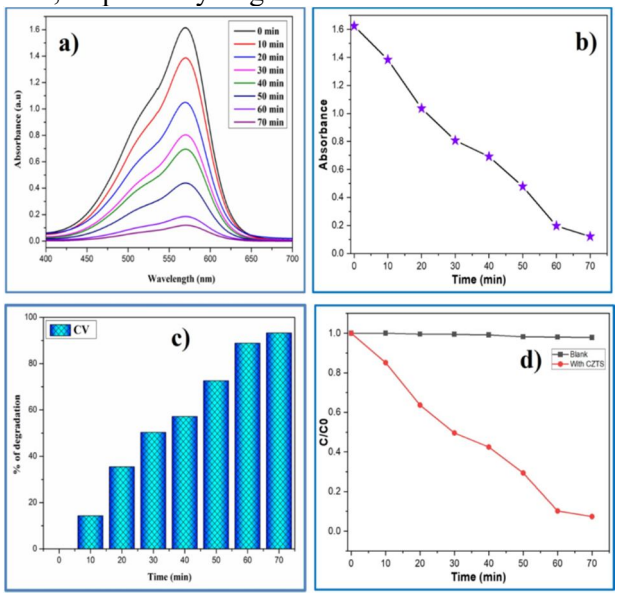

FIG. 8. (a) Absorbance vs wavelength spectra of CZTS TU-10 catalyst for CV dye, (b) absorbance vs irradiation time, (c) degradation efficiency, and (d) C/C_0 vs reaction time.

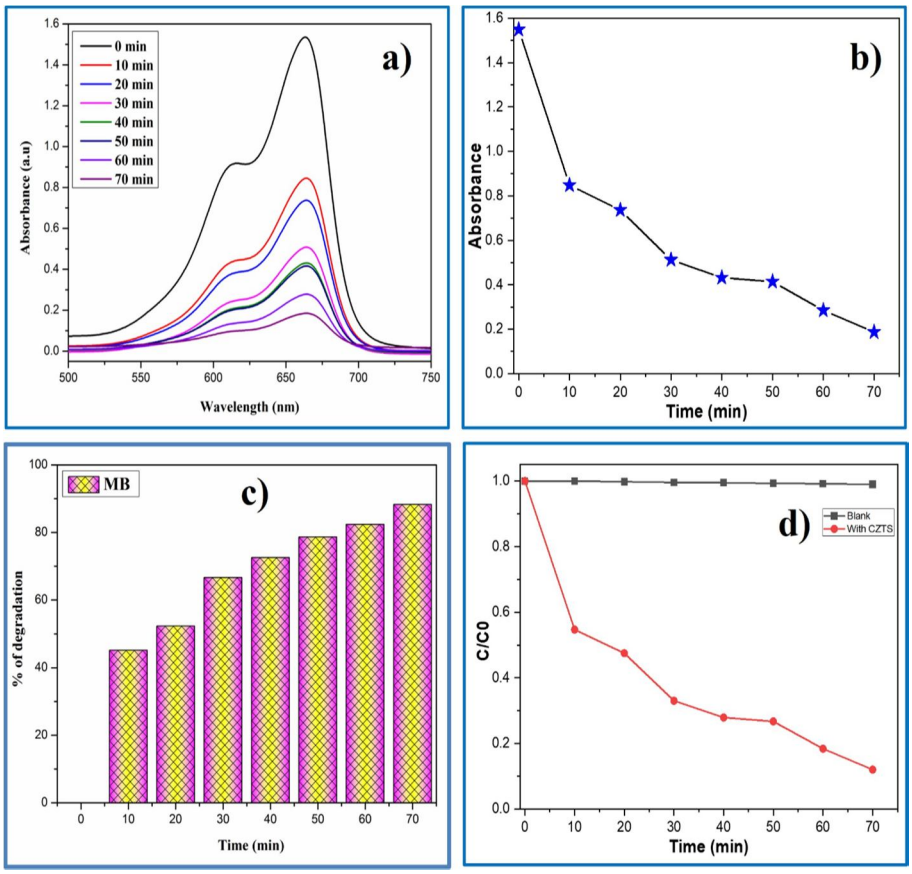

FIG. 9. (a) Absorbance vs wavelength spectra of CZTS TU-10 catalyst for MB dye, (b) absorbance vs irradiation time, (c) degradation efficiency, and (d) C/C_0 vs reaction time.

Moreover, the surfactant-free CZTS nanoparticles produced by the hydrothermal process serve as an efficient photocatalyst for degrading toxic dyes. In a photocatalytic system, a photo-induced molecular transformation occurs on the surface of the photocatalyst. Electrons jump from the valence band to the conduction band when the surface of a photocatalytic material is exposed to energy equal to or greater than the band gap. This causes a negatively charged electron to appear in the conduction band and a positively charged hole to appear in the valence band. The conduction band electron reduces the adsorbed oxygen onto the photocatalytic surface, and the positively charged hole oxidizes the organic contaminants into hydroxyl free radicals.

Table 2 summarizes the photodegradation efficiency of CZTS with previously reported data, prepared by various synthesis processes, as well as their morphology, efficiencies, type of dyes, and degradation rates of dyes. By overall photocatalytic performance, the prepared CZTS TU-10 nanostructures led to a higher degradation rate of MB and CV dyes due to the rose flower-like nanosheet morphology.

TABLE 2. Degradation efficiency of CZTS catalyst with previous studies.

Method	Morphology	Dye	Degradation efficiency / Time (% / min)	Ref
Hydrothermal	Agglomerated	MB	50 / 45	[28]
Hydrothermal	Spherical	RhB	55 / 240	[36]
Hydrothermal	Flower-like	MB	60 / 90	[37]
Hot-injection	Nano-Spheres	pollutants	73 / 150	[38]
Hot-injection	Nano-rods	pollutants	90.3 / 160	[38]
Hydrothermal	Rose-flower like	MB	89 / 70	Present work
Hydrothermal	Rose-flower like	CV	93 / 70	Present work

3.9 Antibacterial Activity

The antibacterial activity of the synthesized CZTS TU-10 nanostructure was carried out against both gram-positive (*Streptococcus pneumoniae, Streptococcus pyogenes*) and gram-negative (*Klebsiella pneumoniae, Vibrio parahaemolyticus*) pathogens. The CZTS TU-10 was tested for its antibacterial properties by using the agar well diffusion method. Figs. 10 (a)-10(d) show the results of the investigation on the antibacterial properties of CZTS nanostructure evaluated by the zone of inhibition (ZOI). Remarkably, following 24 hours of incubation, the synthesized CZTS nanostructures exhibited an inhibition zone around them for all the bacterial strains that were subjected to testing. After incubating the plates for 24 hours at 35℃, the diameter of the inhibitory zones was measured in mm and recorded. The zone of inhibition diameter was calculated corresponding to pathogens, and the values are listed in Table 3. The results revealed that the inhibition of growth increased with increasing concentrations of CZTS. The maximum inhibition zone was obtained against *Vibrio parahaemolyticus* bacteria at 18, 20, 22, and 26 mm, corresponding to 25, 50, 75, and 100 µg/ml.

This observation serves as an indication of the bacteriostatic capability of the CZTS nanostructures. Additionally, the size of the inhibition zone varied depending on the specific type of bacteria [39]. The observed suppression of bacterial growth could be related to the detrimental effects on the bacterial cell membrane and the expulsion of cytoplasmic contents, ultimately leading to the death of the bacterium. The change in the inhibition zone depended on the type of bacteria, the morphology of the nanoparticle, and the behavior of their development.

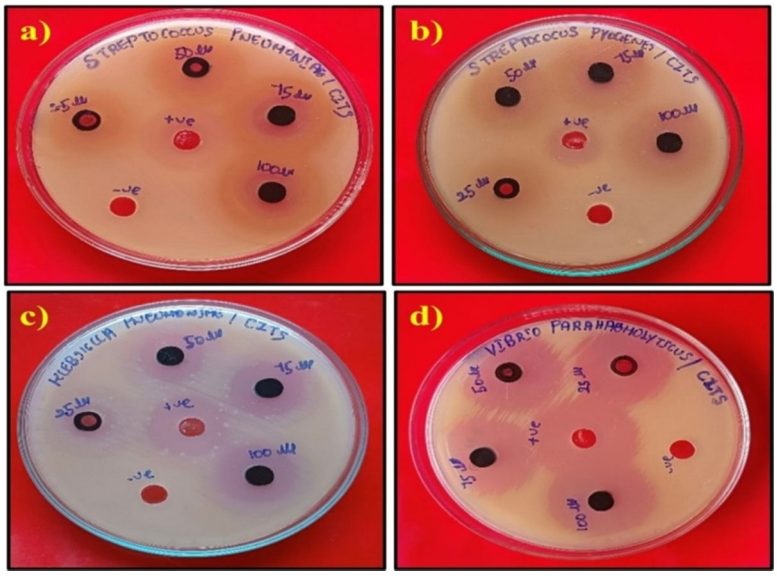

FIG. 10. Antibacterial activity of the CZTS TU-10 nanostructures against (a) *Streptococcus pneumoniae*, (b) *Streptococcus pyogenes*, (c) *Klebsiella pneumoniae*, and (d) *Vibrio parahaemolyticus*.

TABLE 3. Antibacterial activity of CZTS TU-10 nanostructures

S. No	Test Organisms	Zone of inhibition (mm)				
		25 µg/ml	50 µg/ml	75 µg/ml	100 µg/ml	Positive control
1.	*Streptococcus Pneumoniae*	12	14	16	20	26
2.	*Streptococcus Pyogenes*	14	16	18	21	26
3.	*Klebsiella Pneumoniae*	12	14	16	18	26
4.	*Vibrio parahaemolyticus*	18	20	22	26	29

To date, some mechanisms have been suggested for the antibacterial properties exhibited by inorganic nanoparticles. (i) The release of metal cations from nanoparticles leads to interactions with proteins, nucleic acids, and microbial membranes, resulting in structural modifications and inhibition of microbial replication. (ii) The internalization of nanoparticles through ion channels or proteins at the cell wall results in the mechanical breakdown of the cell membrane. (iii) The nanoparticle surface generates reactive oxygen species

(ROS), including hydroxyl radicals (OH), hydrogen peroxide (H_2O_2), and superoxide ($\dot{O_2^-}$). These ROS have the potential to cause significant damage to lipids, DNA, and proteins within the cell membrane, resulting in leakage and degradation of the bacterial cell membrane [40]. Based on this investigation, hydrothermally prepared CZTS TU-10 nanostructures have stronger antibacterial performance against *Vibrio parahaemolyticus* bacteria due to their particle size and better morphology.

4. Conclusion

The pure kesterite phase of CZTS nanostructures was successfully synthesized through a low-cost hydrothermal method without the assistance of surfactants or capping agents by using different concentrations of thiourea. XRD and FT-Raman studies confirmed the growth of pure-phase CZTS nanostructures at higher sulfur concentrations. FESEM studies indicated that different Cu/S ratios had a strong influence on the morphological changes of CZTS. The interplanar distance value was calculated from the HRTEM image and found to be 0.32 nm, which strongly supported the XRD result. The valence states of Cu^{1+}, Zn^{2+}, Sn^{4+}, and S^{2-} were confirmed by XPS. Surfactant-free pure kesterite CZTS TU-10 was found to be a good photocatalyst for CV and MB dyes with degradation efficiencies of 93% and 89% within 70 minutes. The prepared CZTS electrode offered an excellent specific capacity of 389F/g at 10 mV/s by CV measurements. Finally, the surfactant-free CZTS TU-10 sample possessed a flower-like morphology and showed excellent degradation efficiency, better antibacterial activity, and high specific capacitance, all of which revealed that the prepared CZTS nanostructures could be potential candidates for future applications**.**

Acknowledgment

The corresponding author wishes to thank the Head of the Department of Physics and the Centralized Instrumentation and Service Laboratory (CISL), Annamalai University, Annamalai Nagar, Tamil Nādu, India, for providing the CV and analytical instrument facilities.

Funding Information

No funding was received for conducting this study.

Conflict of Interest

The authors declare no conflict of interest.

References

[1] Patil, S.S., Nadaf, S.N., Mali, S.S., Hong, C.K., and Bhosale, P.N., Ind. Eng. Chem. Res., 60 (21) (2021) 7816.

[2] Harinipriya, S., Cassian, H., and Sudha, V., J. Mater. Res. Technol., 15 (2021) 3558.

[3] Patil, U., Dhanasekar, M., Kadrekar, R., Arya, A., Bhat, S.V., and Late, D.J., Ceram. Int., 48 (19) (2022) 28898.

[4] Paraye, A., Ramachandran, M., and Selvam, N.V., Period. Polytech. Chem. Eng., 65(1) (2021) 42.

[5] Saha, S., Int. J. Photoenergy, 2020 (2020) 1.

[6] Qiu, L., Xu, J., Cai, W., Xie, Z., and Yang, Y., Superlattices Microstruct., 126 (2019) 83.

[7] Ahmad, R., Saddiqi, N., and Wu, M., Inorg. Chem., 59 (3) (2020) 1973.

[8] Banerjee, G., Das, S., and Ghosh, S., Mater. Today Proc., 18 (2019) 494.

[9] Engberg, S., Symonowicz, J., Schou, J., Canulescu, S., and Jensen, K.M.Ø., ACS Omega, 5 (18) (2020) 10501.

[10] Vavale, S.D., Pawar, S.G., and Deepti, H., Int. J. Innov. Knowl. Concepts, 6 (11) (2018) 126.

[11] Pathak, M., Bhatt, D., Bhatt, R.C., and Bohra, B.S., Chem. Rec., 24 (1) (2023) e202300236.

[12] Abdel Maksoud, M.I.A., Fahim, R.A., Shalan, A.E., and Abd Elkodous, M.S., Environ. Chem. Lett., 19 (2021) 375.

[13] Tang, Q., Shen, H., Yao, H., Wang, W., Jiang, Y., and Zheng, C., Ceram. Int., 42 (8) (2016) 10452.

[14] Manjula, S., Sarathkumar, A., and Sivakumar, G., J. Nano Res., 79 (2023) 25.

[15] Robati, S.M., Imani, M., and Tadjarodi, Mater. Lett., 225 (2018) 9.

[16] Hirpara, A.B., Chaki, S.H., Kannaujiya, R.M., Khimani, A.J., and Parekh, Appl. Surf. Sci. Adv., 12 (2022) 100338.

[17] Long, B., Cheng, S., Ye, D., Yue, C., and Liao, J., Mater. Res. Bull., 115 (2019) 182.

[18] Mkawi, E.M., Al-Hadeethi, Y., Shalaan, E., and Bekyarova, E., Ceram. Int., 46 (16) (2020) 24916.

[19] Patil, S.S., Mane, R.M., Mali, S.S., Hong, C.K., and Bhosale, P.N., Sol. Energy, 201 (2020) 102.

[20] Shalabayev, Z., Baláz, M., Daneu, N., Kanuchová, M., ... and Burkitbayev, M., ACS Sustain. Chem. Eng., 7 (15) (2019) 12897.

[21] Singh, O.P., Parmar, R., Gour, K.S., Dalai, M.K., Tawale, J., Singh, S.P., and Singh, V.N., Superlatticesand Microstruct., 88 (2015) 281.

[22] Ghosh, A., Biswas, A., Thangavel, R., and Udayabhanu, G., RSC Adv., 6 (98) (2016) 96025.

[23] Rajesh, G., Muthukumarasamy, N., Velauthapillai, D., and Batabyal, S.K., Langmuir, 33 (24) (2017) 6151.

[24] Henríquez, R., Nogales, P.S., Moreno, P.G., Cartagena, E.M., Bongiorno, P.L., Navarrete-Astorga, E., and Dalchiele, E.A., Nanomaterials, 13 (11) (2023) 1731.

[25] Zaman, M.B., Mir, R.A., and Poolla, R., Int. J. Hydrogen Energy, 44 (41) (2019) 23023.

[26] Valdés, M., Pascual-Winter, M.F., and Vázquez, M., Phys. Status Solidi A, 215 (24) (2018) 1800639.

[27] Das, S., Sa, K., Alam, I., and Mahanandia, P., Mater. Lett., 232 (2018) 232.

[28] Phaltane, S.A., Vanalakar, S.A., Bhat, T.S., Patil, P.S., Sartale, S.D., and Kadam, L.D., J. Mater. Sci. Mater. Electron., 28 (2017) 8186.

[29] Baid, M., Hashmi, A., Jain, B., Singh, A.K., Susan, M.A.B.H., and Aleksandrova, M., Opt. Quantum Electron., 53 (2021) 1.

[30] Padhy, S., Mannu, R., and Singh, U.P., Sol. Energy, 216 (2021) 601.

[31] Zhao, Y., Yan, J., Huang, Y., Lian, J., Qiu, J., Bao, J., Cheng, M., Xu, H., Li, H., and Chen, K., J. Mater. Sci. Mater. Electron., 29 (2018) 11498.

[32] Premkumar, V.K., Sivakumar, G., Dinesh, S., and Barathan, S., J. Mater. Sci. Mater. Electron., 28 (2017) 4780.

[33] Farzi, M., Moradi, M., Hajati, S., Toth, J., and Kazemzadeh, A., Synth. Met., 278 (2021) 116815.

[34] Sarkar, S., Howli, P., Das, B., Das, N.S., Samanta, M., Das, G.C., and Chattopadhyay, K.K., ACS Appl. Mater. Interfaces, 9 (27) (2017) 22652.

[35] Selvam, M., Sivakumar, G., and Ayyar, M., Z. Phys. Chem., 0 (2024).

[36] Sawant, J.P., Rajput, R., Patil, S., Ryu, J., Patil, D.R., and Kale, R.B., J. Mater. Sci. Mater. Electron., 32 (2021) 22803.

[37] Sheebha, I., Venugopal, V., James, J., Maheskumar, V., Sakunthala, A., and Vidhya, B., Int. J. Hydrogen Energy, 45 (15) (2020) 8139.

[38] Semalti, P., Sharma, V., and Sharma, S.N., J. Materiomics, 7 (5) (2021) 904.

[39] Hirpara, A.B., Chaki, S.H., Kannaujiya, R.M., Khimani, A.J., Appl. Surf. Sci. Adv., 12 (2022) 100338.

[40] Ocakoglu, K., Dizge, N., and Colak, S.G., Colloids Surf. A Physicochem. Eng. Asp., 616 (2021) 126230.